A study on a tidal rotor under the combined effects of currents and regular waves using Actuator-Line CFD simulations

Federico Zilic de Arcos, James McNaughton, Christopher R. Vogel, and Grégory Pinon

Abstract—**This paper presents an analysis of a tidal rotor under the combined effects of a steady current and surface waves. Five different regular waves were simulated using a Reynolds-Averaged Navier-Stokes computational fluids dynamics model with a k-ω SST turbulence closure model, a Volume of Fluid model of the free surface, and an actuator line representation of the rotor. The implemented model shows the hydrodynamic interactions between the rotor and the surrounding flow boundaries, as well as a significant impact of the waves on rotor thrust, power, and wake development. The results show that while there is a modest impact of the waves on mean thrust and power, a significant impact on thrust and power fluctuations was observed, with fluctuations an order of magnitude greater than the changes in mean quantities. Variations in phase-averaged blade loads as a function of azimuthal position were also observed, with fluctuations concentrated near the free surface but also a function of wave frequency. Waves were also found to cause changes in wake development downstream of the rotor, with the formation of large vortex structures that depended on wave frequency.**

Index Terms—**Tidal rotor, waves, volume of fluid, CFD, actuator line**

I. INTRODUCTION

TIDAL rotors deployed at sea are likely to be affected by turbulence, shear, surface waves, and wave-induced motions in the case of floating devices. These can induce significant fluctuations in rotor thrust and power in addition to hydrodynamic blade loads, as well as impact the design of the rotor [1].

Surface waves have the potential to be the largest driver of load and power fluctuations on tidal rotors [2]. Several experimental studies have reported substantial thrust and power fluctuations due to wave action: Galloway et al. [3] reported fluctuations in the median flapwise root bending moment on a blade of up to 175%; while Draycott et al. [4] reported fluctuations about the mean between 7% and 65% for integrated thrust, and 13% to 165% for power. Several other studies report load and power fluctuations of the same order of magnitude (see, e.g., Barltrop et al. [5], Faudot and Dahlhaug [6], Gaurier et al. [7], Guo et al. [8], Dufour et al. [9], or Watanabe et al. [10]). Most of these studies also indicate that time-averaged loads are largely unaffected by the combination of waves and homogeneous currents. The magnitude of the effects of surface waves on tidal rotors, however, is strongly case-dependent and is influenced by factors such as wave amplitude, frequency, incidence angle, and the rotor's submergence depth, as they alter the flow profile that the turbine is exposed to [8] [11].

Blockage, understood as the interaction between the rotor and the surrounding boundaries of the fluid domain, is also likely to affect rotor loads and power performance. The simplest form of blockage is the isotropic interaction between a rotor and the boundaries constraining the flow domain [12]. The effects of this isotropic blockage are normally seen in the form of an increase in maximum thrust and power on tidal turbines due to a change in the static pressure distribution around the rotor which can lead to an associated increased mass flux through the rotor. This also affects the relationship between thrust and axial induction commonly used in Blade-Element Momentum models [13].

Realistic scenarios, however, include more complex phenomena such as the non-isotropic interaction of a rotor and the free-surface [11], as well as the interactions between multiple rotors [14], [15]. Anisotropic blockage creates bypass zones where the flow is accelerated, creating a non-uniform flow field that affects rotor loads, power, and wake development [16]. Even if the flow field is steady, the rotation of the blades results in a "sampling effect" as they pass by flow boundaries that will result in transient load fluctuations [17].

The effects of waves and non-isotropic interactions between the rotor and the free surface are presented in this work. Our paper discusses the case of a tidal rotor operating in close proximity to the free surface and a lateral symmetry plane to model dual-rotor operation, under the effects of a steady homogeneous current and regular waves. We used an actuator-line representation of the rotor blades embedded within a multiphase Reynolds-Averaged Navier-Stokes (RANS) Computational Fluid Dynamics (CFD) model.

II. METHODS

A. Rotor characteristics and analysed cases

A tidal rotor designed by Cao [18] was used in this study. This is a 1.2 m diameter tidal rotor designed for multi-rotor operation. The rotor was designed using an

F. Zilic de Arcos and G. Pinon are with the Laboratoire Ondes et Milieux Complexes, UMR 6294 CNRS, France (e-mail: federico.zilic@univ-lehavre.fr).

James McNaughton is with MARIN, Wageningen, The Netherlands (e-mail: j.mcnaughton@marin.nl)

C. R. Vogel is with the Engineering Department, University of Oxford, United Kingdom (e-mail: christopher.vogel@eng.ox.ac.uk)

Digital Object Identifier:
https://doi.org/10.36688/ewtec-2023-367

FX-84-W-140 hydrofoil modified with a blunt trailing edge through the application of a uniform thickening function to the suction and pressure surfaces on the rear portion of the foil. The hydrofoil has an optimum angle of attack of approximately 6 degrees. A RANS-Blade Element (BE) based design method [18] was used to design the rotor for maximum performance at a tip-speed ratio $\lambda = \omega R/U_\infty = 6.2$, where ω is the rotational speed of the rotor, R is the blade tip radius, and U_∞ is the undisturbed flow speed in the absence of waves.

The rotor design exploits local blockage and constructive interference effects [14] through an increased rotor solidity and reducing the variation in blade twist. This results in an increased power production compared to an unblocked rotor design [19]. Further optimisation, using blade-resolved simulations, allowed for additional performance increases by tuning the local thrust coefficient along the blades [18]. The numerical methods and the concept of constructive interference were examined and validated by McNaughton et al. in experimental campaigns performed in a flume [20] and a towing tank [15]. The experiments demonstrated that turbine power could be increased through constructive interference by closely spacing the turbines whilst maintaining the same overall blockage within the respective test facilities.

The rotor was modelled in the present study operating at a fixed tip-speed ratio of $\lambda = 6.2$, relative to the undisturbed current, set to a speed $U_\infty = 1$ m/s, with a turbulent intensity of 0.6% and a length scale of 0.003 metres defined at the inlet. The rotor was placed inside the simulated domain at a lateral distance of $D/8$ from a symmetry plane, where D is the rotor diameter. The symmetry plane emulates the multi-rotor operation described by Cao [18] with an inter-turbine (tip-to-tip) spacing of $D/4$ whilst allowing only one rotor to be simulated. This implies that the turbines are contra-rotating. The tip clearance was set to $D/3$ with respect to the free surface following McNaughton et al. [20], while the tank depth was set to 5.4 metres. Two-dimensional hydrofoil polar coefficients for the Actuator Line (AL) model were reproduced from Cao [18] to match the inputs used for the design of this rotor.

Five cases with regular waves were simulated with a targeted amplitude of 0.1 m and wavelengths $L \in \{9.76, 6.25, 4.34, 3.70, 3.01\}$ m. These correspond to nominal wave frequencies, without accounting for the current-related Doppler shift, of 0.40, 0.50, 0.60, 0.65, and 0.72 Hz, respectively. The nominal frequencies are used to label the different cases for analysis, and can be seen in table I compared to the encounter frequencies (frequencies relative to the rotor reference frame) and the corresponding wavelengths.

The complete study consists of 11 simulations: five cases to study the flow conditions where the tank is simulated with waves and current but without the rotor; five cases with the rotor operating with waves and currents; and one case with the rotor operating only under the effects of a steady current. The simulations were each performed for 60 seconds, accounting for nearly 100 blade rotations. The simulated time was set to obtain full wake development and the convergence of the cycle-averaged power and thrust coefficients (approximately 20 seconds) while providing sufficient data after for the analysis of blade forces and fluctuations across the entire azimuth.

TABLE I
CORRESPONDENCE BETWEEN NOMINAL WAVE FREQUENCIES, ENCOUNTER FREQUENCIES RELATIVE TO THE ROTOR, AND WAVELENGTHS

Nominal frequency f [Hz]	**Encounter frequency** f_e [Hz]	**Wavelength** L [m]
0.40	0.50	9.76
0.50	0.66	6.25
0.60	0.83	4.34
0.65	0.92	3.70
0.72	1.05	3.01

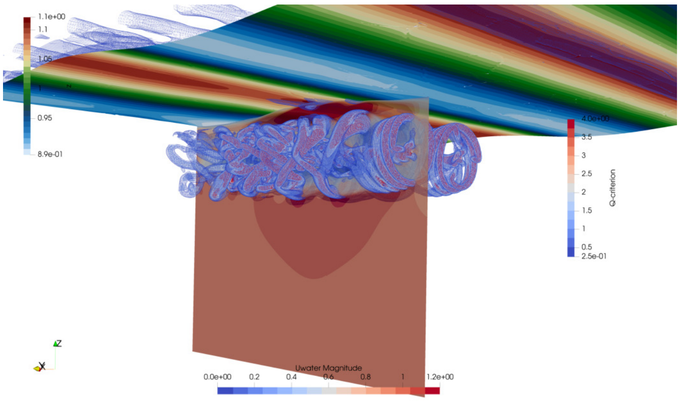

Fig. 1. Three-dimensional visualisation of one of the simulated cases. The render presents isocontours of Q-criterion, the free surface, and the velocity field on a vertical plane. The visualisation of the second rotor is recreated through a reflection of the modelled field.

B. CFD model

We used the open-source code OpenFoam v2012 to perform our simulations with an incompressible RANS-CFD model, an actuator line representation of the rotor, a Volume of Fluid (VoF) model for the free surface, and a stabilised k-ω SST turbulence closure model.

The actuator line model works as a virtual representation of the turbine wherein the rotor blades are modelled as a series of collocation points along lines that move in time where the blades would be placed. Sectional forces, centred at each collocation point, are applied to the flow as a momentum source, smeared out using a Gaussian distribution for the numerical stability of the scheme. The forces are calculated based on tabulated lift and drag coefficients. In this study, we used polar coefficients calculated using a two-dimensional RANS CFD model, sourced from Cao [18], and corrected for tip-loss effects using the model of Wimshurst [21]. To calculate the forces, the local flow at each collocation point is used to determine the sectional angle of attack and inflow speed.

The local flow is determined using the line-average method of Jost et al. [22], a robust flow-sampling technique for rotor-blade simulations [23], and implemented within the AL model according to Zormpa et al. [24]. Compared to the original method of sampling the flow at the collocation point [25], the line-average method within the AL model increases model robustness by reducing the sensitivity of thrust and power to the size of the force smearing Gaussian distribution, as well as temporal and spatial discretisations of the domain and numerical scheme. The methodology also avoids the underestimation of axial induction obtained when sampling inside the region where the forces are applied. Meyer Forsting et al. [26] attribute the underestimation of axial induction, by comparing the actuator points to a vortex core, to the viscous damping that limits the induced velocity and the magnitude of the shed vorticity. In this AL implementation, the flow sampling occurs outside the force Gaussian, thus avoiding the underestimation of axial induction [24] without requiring corrections such as the one proposed by Meyer Forsting et al. [26].

We used the stabilised k-ω SST turbulence closure model of Larsen and Fuhrman [27]. This modification of the original k-ω SST model [28] introduces an extra limiter on the production of the specific dissipation rate, ω, to stabilise the over-production of turbulent kinetic energy in regions of nearly-potential flow [27]. The use of this modified turbulence closure model reduces the wave damping commonly observed in RANS models.

The fluid domain was set to 13 metres long, and was discretised with isotropic hexahedral cells and a one-level isotropic refinement zone. The background mesh size was set to 0.04 metres, and 0.02 metres in the refined zones. The refined region spans two wave heights above and two wave heights below the mean free surface, following Windt et al. [29], and a box covering the surroundings of the rotor (one diameter upstream, four diameters downstream, and one diameter in each Cartesian direction normal to the rotor plane). For the rotor, this mesh size corresponds to 60 cells per diameter. For the waves, the discretisation resolves 10 cells per wave height and a minimum of 150 cells per wavelength for the shortest analysed wave. The mesh resolution allows for the numerical damping of waves to remain low [29] and for the forces on the rotor not to be affected by the grid size [24] [30]. The resulting domain consists of 11.4 million cells.

The timestep was set to 0.0025 seconds, leading to a maximum Courant number of approximately 0.40 and ensuring that the tip of the actuator line does not move more than one cell per timestep, as is typically recommended for AL methods [24]. We used second-order discretisation schemes for velocity, gradients and volume fraction, first-order for turbulence scalars, and a PISO algorithm for pressure-velocity coupling.

The OpenFoam wave generation and absorption toolbox waves2Foam was used (Jacobsen et al. [31]) with the Generating-Absorbing Boundary Conditions (GABC) of Borsboom and Jacobsen [32] to minimise wave reflections. Waves were generated using the stream function wave theory described by Fenton [33]. This is a non-linear model of a steady wave that is defined relative to an undisturbed current. The main parameters used to define the waves are the wave height, depth, and wavelength (see table I).

A three-dimensional representation of results produced with the numerical model can be seen in Fig. 1.

III. Results and discussion

A. Interactions between the rotor and domain boundaries

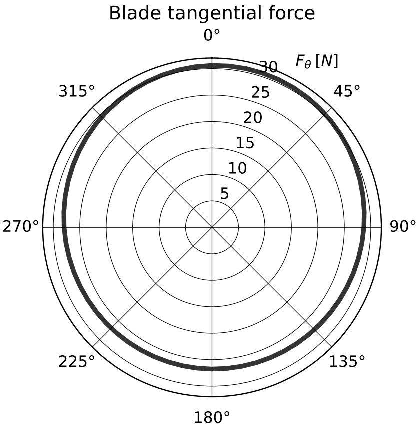

Fig. 2. Azimuthal distribution of the time-averaged tangential force on one blade of the rotor operating under a steady current speed $U_\infty = 1.0$ m/s and with no waves. The rotor is centred $D/3$ from the free surface at 0°, and $D/8$ from the central symmetry plane at 90°. The direction of blade rotation is clockwise.

Fig. 2 shows the tangential force as a function of azimuthal position for one of the rotor blades operating under a steady current with a speed of $U_\infty = 1.0$ m/s. In this figure, 0° and 90° correspond to the sides next to the free surface and symmetry plane, respectively. The results in this figure agree with the observations presented by McNaughton et al. [15] regarding the azimuthal asymmetry of the loads, with higher forces next to the symmetry plane and free surface due to the constructive interference effects. This occurs due to the flow confinement next to these boundaries, leading to flow acceleration on the bypass and higher through-rotor mean flow speeds, as shown in Fig. 3. The flow acceleration leads to higher angles of attack and relative speed, consequently generating larger thrust and tangential forces as the blade passes next to the boundaries; this is discussed further below.

The asymmetry in the tangential force is observed both on the vertical and horizontal planes. The highest loads are observed on the quadrant between the symmetry plane and the free surface. Despite the modelling conditions not being directly comparable, these observations are consistent with the results presented by McNaughton et al. [15] for the outboard turbine on a 4-rotor array.

B. Wave effects on rotor thrust and power performance

Whole-rotor performance is quantified in terms of the thrust and power coefficients, C_T and C_P respectively. The coefficients are defined to normalise the rotor thrust T and power P in terms of the undisturbed

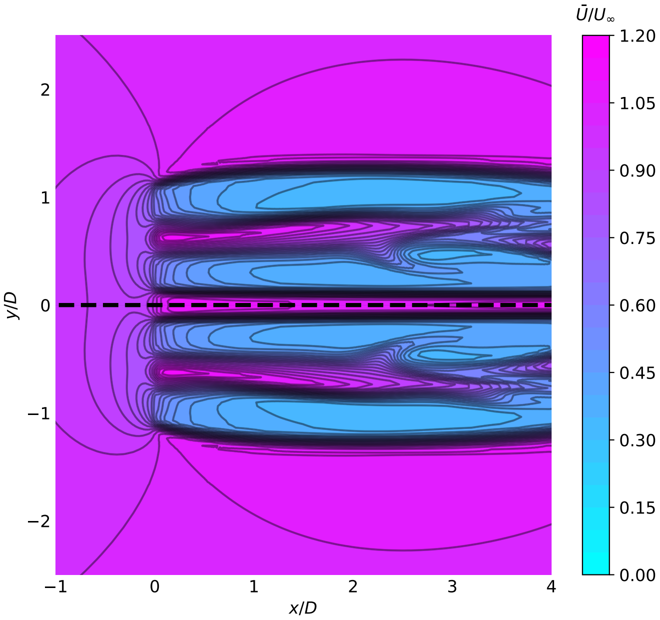

Fig. 3. Contours of time-averaged flow speed through a rotor-centred horizontal plane. The rotor is operating without waves. The current flows from left to right with a bulk flow speed of 1.0 m/s. The central symmetry plane is highlighted with a black dashed line and data is reflected with respect to this plane to show the two rotors.

momentum and energy flux respectively in the absence of waves:

$$C_T = \frac{T}{\frac{1}{2}\rho U_\infty^2 A} \tag{1}$$

$$C_P = \frac{P}{\frac{1}{2}\rho U_\infty^3 A} \tag{2}$$

where ρ is the fluid density and $A = \frac{1}{4}\pi D^2$ is the swept area of the rotor. Fig. 4 shows the integrated rotor thrust and power coefficients for the different wave frequencies that were analysed. The figure highlights the time-averaged quantities over the last 10 wave periods, as well as a measure of transient fluctuations in this time window determined by two standard deviations.

In agreement with previous studies, the integrated loads show only a very small impact of the waves on mean thrust and power. Particularly, we observe maximum deviations from the case with no waves in the order of 3.3% and 0.4% for mean power and thrust, respectively. The results also show significant load fluctuations in C_T and especially C_P, with two standard deviations corresponding to up to 11.9% and 37.5% of the wave-free thrust and power, respectively, at a wave frequency of 0.4 Hz.

Fig. 5 shows the azimuthal distribution of the time-averaged and fluctuations of thrust and torque for one blade over ten wave periods. Fluctuations are represented by the mean value plus/minus two standard deviations. These results show a comparison of two wave frequencies, 0.50 and 0.65 Hz.

The figure shows that the mean thrust and torque as functions of azimuthal position show similar trends to those presented previously for the integrated loads. The cases with waves show small differences in mean forces compared to the case without waves, with only a marginal increase in torque and thrust in the region close to the free surface. This explains the minor differences observed previously in integrated loads. The results also suggest that the constructive interference effects (load and power changes near the symmetry plane and free surface) are not significantly affected by the presence of waves when loads are averaged in time.

Fig. 5 also shows that the cases with waves are affected by large thrust and torque fluctuations, with the 0.50 Hz wave showing larger fluctuations than the 0.65 Hz wave for all azimuthal locations. These fluctuations, presented in terms of standard deviations, are a consequence of the different frequencies of waves and blade rotation. From a blade-element perspective, the blade samples a velocity field that changes not only with wave frequency but also with the depth-dependant amplitude of wave kinematics. This affects the blades, which show a concentration of load fluctuations near the free surface in the region where wave kinematics are stronger. Despite both cases with waves

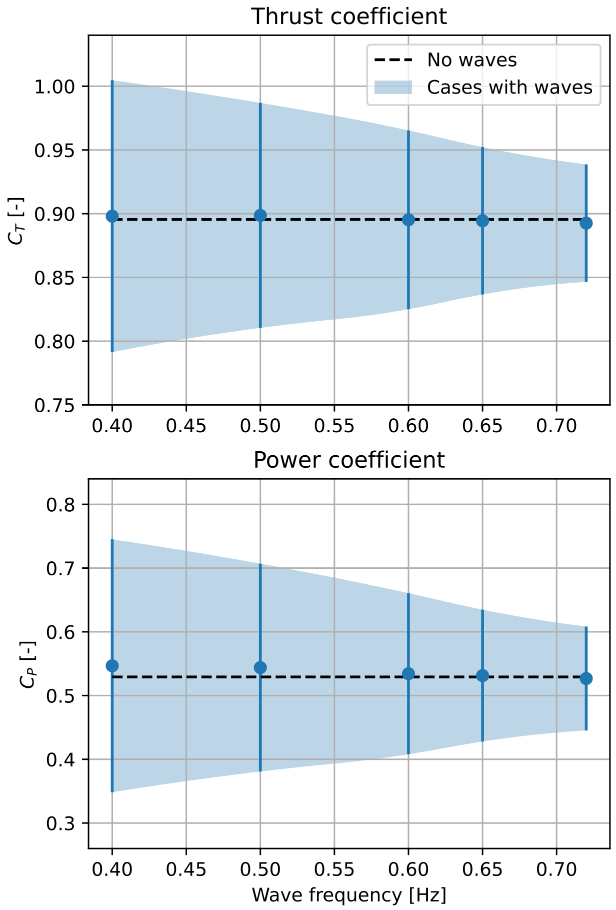

Fig. 4. Time-averaged and transient fluctuations on the integrated thrust and power coefficients (C_T and C_P, respectively) for the rotor under different wave conditions. The bullet points show time-averaged quantities, while the shaded area represents two standard deviations of the metrics. The dashed black line marks the results without waves.

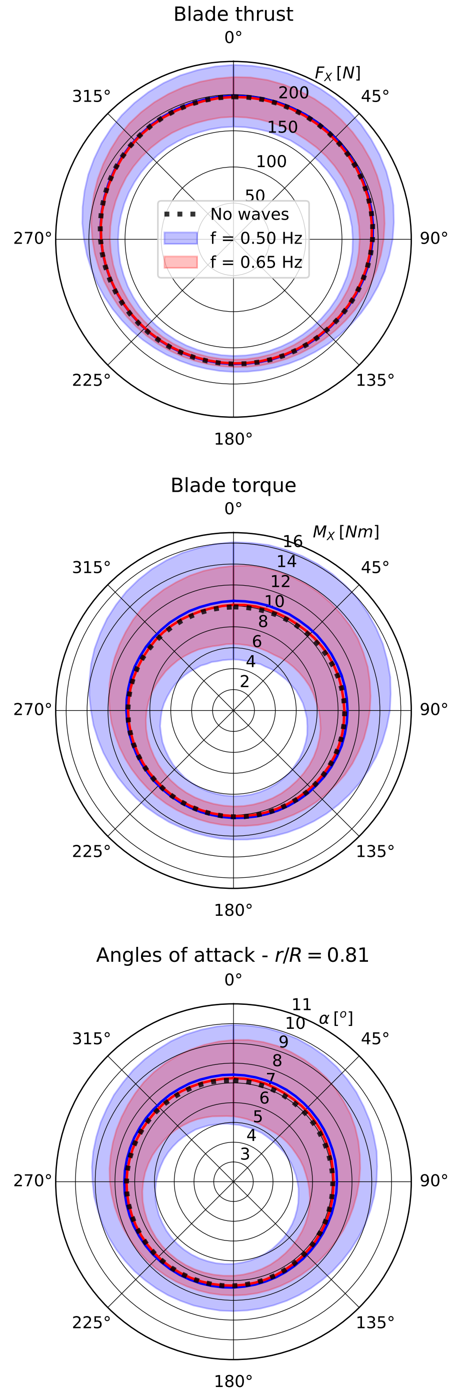

Fig. 5. Polar distributions of thrust, torque, and angle of attack on a blade for the rotor subject to different wave conditions. Thrust and torque are blade-integrated, while the angles of attack correspond to a blade section at $r/R = 0.81$. The lines shows the time-averaged values for each azimuthal location, while the shaded areas show two standard deviations from the mean. 0° and 90° correspond to the closest points to the free surface and symmetry plane, respectively. The direction of blade rotation is clockwise.

showing a top-to-bottom asymmetric distribution in force fluctuations, the shorter wave produces a larger difference between the 0° and 180° positions. This is linked to a steeper decay of wave kinematics with depth for shorter waves.

The trends observed for the blade forces are a consequence of changes in the flow, and can also be observed on the sectional angles of attack in Fig. 5. The polar distribution of angles of attack corresponds to a blade section at $r/R = 0.81$. This is normally the region of the blade where the maximum thrust and torque can be found and is considered representative of the entire blade.

The angle of attack plot shows a marginal increase in time-averaged angles of attack near the free surface for the cases with waves compared with the case without, suggesting higher through-rotor mean speeds. The largest angle of attack fluctuations, however, occur not exactly at the top dead centre but at approximately 15°. This is caused by the interactions between the waves and the symmetry plane. The trend is also visible on the loads but is less evident, which is a consequence of the analysed section being close to the tip. The near-tip sections, due to their proximity to the symmetry plane, are more likely affected by constructive interference effects than sections closer to the root of the blade.

C. *Wave effects on the flow field*

Fig. 6 shows the time-averaged flow speed through a vertical plane for two wave conditions and the case without waves. The plot shows the flow acceleration in the bypass formed between the rotor and the free surface, as well as a high-speed jet at the centre of the rotor due to the lack of a nacelle being present in the numerical model to block the flow.

The wake is vertically asymmetric about the rotor centreline for all cases. The free-surface proximity at the top limits the momentum available for exchange with the wake, slowing down the wake recovery of the top region compared with the bottom side of the rotor, producing the asymmetric shape observed in the plots.

The waves also affect wake development by increasing the mixing both inside the wake and between wake and outer flow. Internal flow structures, such as the central jet, are mixed with the rest of the wake earlier in the cases with waves. In the figure, the central jet remains visible on the case without wave until approximately three diameters, while in the cases with waves, it is not distinguishable from the rest of the flow from approximately 2 diameters from the rotor plane.

In the velocity contours of Fig. 6, the edge between the wake and the outer flow, for the cases with waves, also displays gentler velocity gradients than the case without waves, especially from $1D$ downstream of the rotor. Wake mixing in the no-wave case is a predominantly shear-driven process, concentrated in regions with large velocity gradients. The spreading of the wakes just downstream of the turbines in the waves cases suggests that waves can also play an important role in inducing a faster wake recovery behind turbines. This phenomenon has implications for the layout

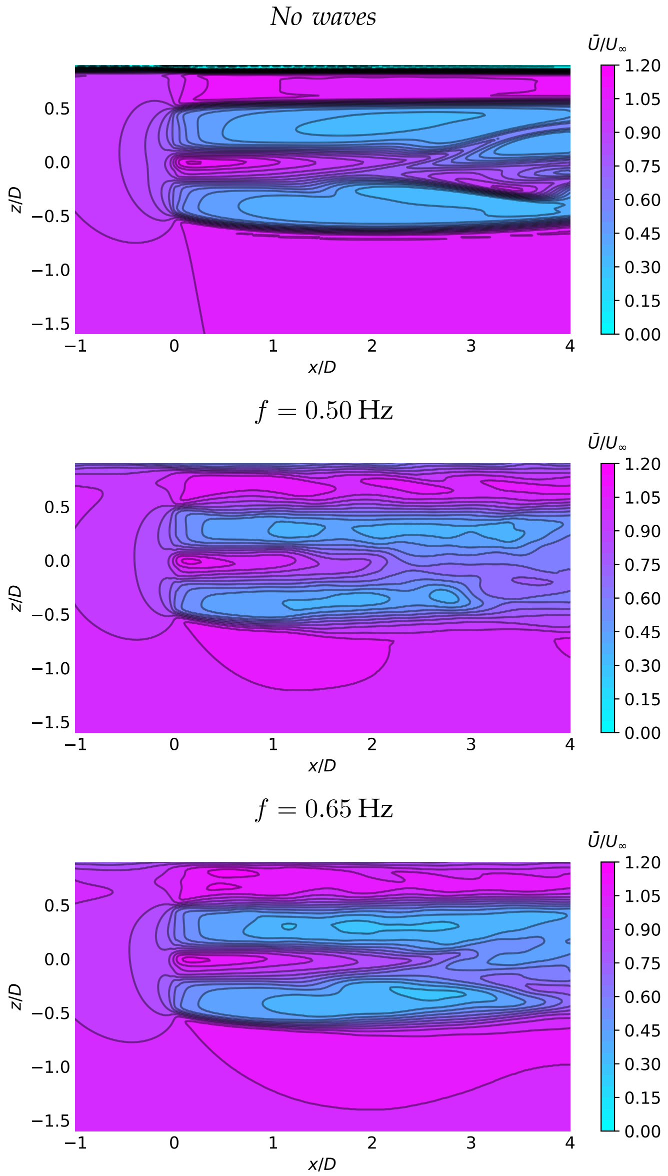

Fig. 6. Time-averaged flow speed through a rotor-centred vertical plane for three different cases: no waves (top), wave frequency 0.5 Hz (middle) and wave frequency 0.65 Hz (bottom). The flow speeds are normalised by the undisturbed current U_∞. The flow is from left to right and the mean free surface position is at the top of each figure.

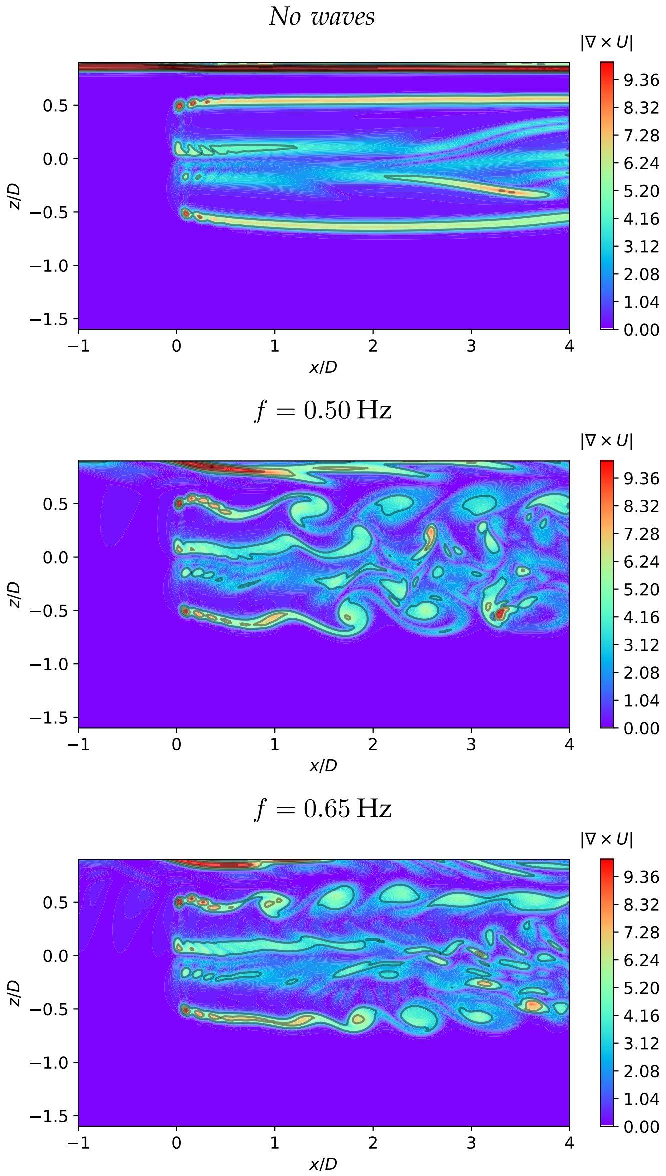

Fig. 7. Instantaneous contours of vorticity magnitude on a rotor-centred vertical plane for three wave conditions: no waves (top), wave frequency 0.5 Hz (middle) and wave frequency 0.65 Hz (bottom). The flow is from left to right and the mean free surface position is at the top of each figure.

and operation of staggered turbines and tidal turbine arrays [10]. The strength of the mixing process can also be observed in the instantaneous vorticity contours in Fig. 7.

The instantaneous flow fields show further details of the interactions between the rotor and the waves. Fig. 7 shows the magnitude of the vorticity on a vertical plane across the rotor, for three different wave conditions. While the plot shows a continuous vortex sheet formed from the tip vortices for the case without waves, the results show the formation of large vortical structures in the cases with waves. These instabilities are a consequence of the interaction between the turbine's shed vorticity, the wave field, and the shear between the rotor wake and the outer flow.

Fig. 8 shows three-dimensional isocontours of Q-criterion for all wave cases. The plot without waves only shows the tip vortices, which extend no further than approximately one and a half diameters, and the large structure formed by the root vortices and the central jet. The cases with waves, however, show the formation of large vortex structures that travel across the entire simulated domain. These vortices, much larger in size than the tip vortices, correspond to the large structures observed in the vorticity plane. Their three-dimensional shape, however, is more complex than the two-dimensional vorticity planes display. The formation of these structures occurs due to several tip-shed vortex filaments being merged and pumped downstream by the periodic inflow and outflow oscillations that are induced by the passing waves. The process is enhanced by the wave-induced vertical velocity fluctuations affecting the vorticity sheet and interacting with the shear layer between the wake and the outer flow. This creates structures that are much larger in

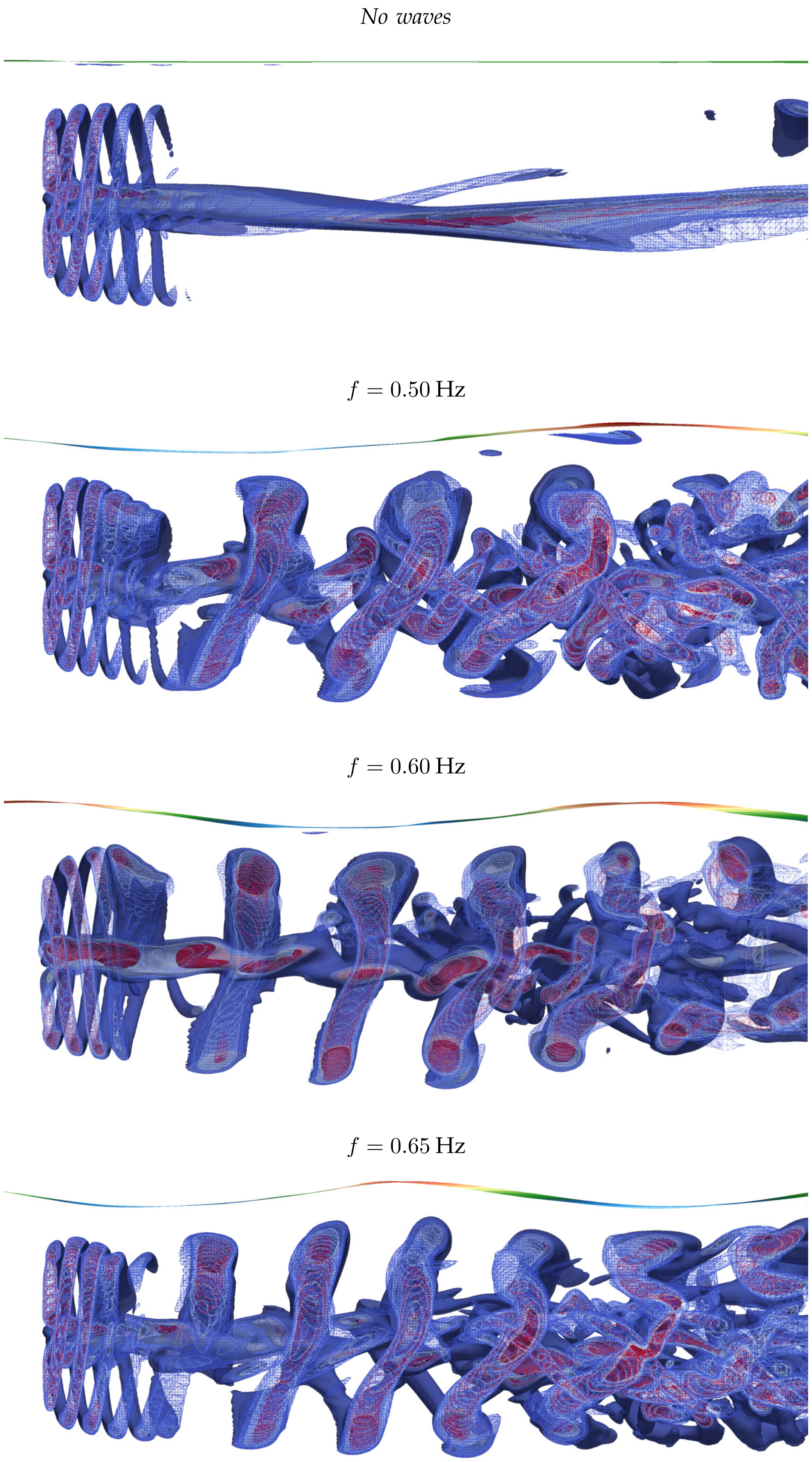

Fig. 8. Instantaneous contours of Q-criterion downstream of the rotor for four different wave conditions: no wave (top), and wave frequencies of 0.4 Hz (centre top), 0.5 Hz (centre bottom), and 0.6 Hz (bottom). The flow is from left to right, and the free surface is also visible.

size than the originating filaments, and form different patterns depending on the wave conditions and rotational frequency. In this limited set of simulations, we observed the formation of at least two distinct patterns: a continuous helical vortex ($f = 0.50\,\text{Hz}$ and $f = 0.65\,\text{Hz}$), and sets of independent vortex rings ($f = 0.60\,\text{Hz}$).

IV. CONCLUSION

The combined effects of waves and currents on tidal turbines can lead to significant fluctuations in turbine and blade loads. This study has employed an actuator line turbine representation to investigate the performance of a tidal rotor close to a free surface.

Our results are consistent with previous experimental research, showing that time-averaged thrust and power on a tidal rotor are not substantially affected by the combined effects of waves and currents. Our results can further extend this conclusion, supporting that this occurs not only at integrated load level, power and thrust coefficients, but also on an individual blade basis. The phase-averaged loads over the blade azimuth show no substantial differences between the cases with waves and the one without for the entire rotation.

Despite the limited impact on mean loads, load fluctuations are significant. We observed the impact of waves, which induced fluctuations in power and thrust coefficients of up to 37.5% and 11.9%, respectively, for the lowest-frequency wave analysed in our study. These fluctuations have an asymmetric distribution over the azimuth as a consequence of the decay of wave kinematics, with a greater load asymmetry throughout a blade rotation for shorter waves but larger load fluctuations across the entire azimuth for the longer waves.

The flow field also showed differences between cases. Waves increase the rate of wake mixing downstream of the turbine through an increased momentum exchange between the wake and the outer flow. The interaction between the wake and the waves also induces the formation of three-dimensional vortex structures. The shape of these 3D structures was identified to be a function of wave characteristics as well as rotor design and operational conditions, displaying the formation of helical filaments or independent vortex rings.

The study, however, is not to be regarded as definitive. The limitations of RANS VoF models regarding the damping of wave height and kinematics are well described in the literature. Using a single mesh domain to study all cases means that numerical damping will affect the less resolved waves, i.e., those shorter waves with fewer cells per wavelength will be the most affected. Higher-order turbulence models are also required to further study wake and wave interactions, a study that is currently under development. Future studies will also be conducted to validate the numerical approach presented herein and to determine the impact of numerical discretisation and modelling on the resolution of waves interacting with tidal turbines.

ACKNOWLEDGEMENT

This project received funding from the European Union's Horizon 2020 research and innovation programme under the Marie Skłodowska-Curie grant agreement No 101034329, recipient of the WINNING-Normandy Program supported by the Normandy Region. This work was funded as part of the Tidal Stream Industry Energiser Project (TIGER), a European Union INTERREG V A France (Channel) England Research and Innovation Programme, which is co-financed by the European Regional Development Fund (ERDF). CRV acknowledges the support of the UKRI through his Future Leaders Fellowship MR/V02504X/1. The computations in the present work were performed on computing resources provided by CRIANN (Normandy, France)

REFERENCES

[1] T. A. A. Adcock, S. Draper, R. H. J. Willden, and C. R. Vogel, "The fluid mechanics of tidal stream energy conversion," *Annual Review of Fluid Mechanics*, vol. 53, pp. 287–310, 2021.

[2] G. T. Scarlett and I. M. Viola, "Unsteady hydrodynamics of tidal turbine blades," *Renewable Energy*, vol. 146, pp. 843–855, 2020.

[3] P. W. Galloway, L. E. Myers, and A. S. Bahaj, "Quantifying wave and yaw effects on a scale tidal stream turbine," *Renewable Energy*, vol. 63, pp. 297–307, 2014.

[4] S. Draycott, G. Payne, J. Steynor, A. Nambiar, B. Sellar, and V. Venugopal, "An experimental investigation into non-linear wave loading on horizontal axis tidal turbines," *Journal of Fluids and Structures*, vol. 84, pp. 199–217, 2019.

[5] N. Barltrop, K. S. Varyani, A. Grant, D. Clelland, and X. P. Pham, "Investigation into wave-current interactions in marine current turbines," *Proceedings of the Institution of Mechanical Engineers, Part A: Journal of Power and Energy*, vol. 221, no. 2, pp. 233–242, 2007.

[6] C. Faudot and O. G. Dahlhaug, "Prediction of wave loads on tidal turbine blades," *Energy Procedia*, vol. 20, pp. 116–133, 2012.

[7] B. Gaurier, P. Davies, A. Deuff, and G. Germain, "Flume tank characterization of marine current turbine blade behaviour under current and wave loading," *Renewable Energy*, vol. 59, pp. 1–12, 2013.

[8] X. Guo, J. Yang, Z. Gao, T. Moan, and H. Lu, "The surface wave effects on the performance and the loading of a tidal turbine," *Ocean Engineering*, vol. 156, pp. 120–134, 2018.

[9] M.-A. Dufour, G. Pinon, B. Gaurier, G. Germain, J.-V. Facq, M. Togneri, F. Represas, E. Nicolas, and J. Marcille, "Comparison of the experimental response of two horizontal axis tidal turbines to wave and current from a frequency dependency point of view," *Trends in Renewable Energies Offshore*, pp. 123–132, 2022.

[10] S. Watanabe, M. M. Kamra, and C. Hu, "An experimental study of surface wave effects on two interacting tidal turbines," *Journal of Marine Science and Technology*, pp. 1–12, 2023.

[11] N. Kolekar, A. Vinod, and A. Banerjee, "On blockage effects for a tidal turbine in free surface proximity," *Energies*, vol. 12, no. 17, p. 3325, 2019.

[12] H. Glauert, *The elements of aerofoil and airscrew theory*. Cambridge University Press, 1947.

[13] F. Zilic de Arcos, "Hydrodynamics of highly-loaded axial flow tidal rotors," Ph.D. dissertation, University of Oxford, 2021.

[14] T. Nishino and R. H. J. Willden, "The efficiency of an array of tidal turbines partially blocking a wide channel," *Journal of Fluid Mechanics*, vol. 708, pp. 596–606, 2012.

[15] J. McNaughton, S. Ettema, F. Zilic de Arcos, C. Vogel, and R. Willden, "An experimental investigation of the influence of inter-turbine spacing on the loads and performance of a coplanar tidal turbine fence," *Journal of Fluids and Structures*, vol. 118, p. 103844, 2023.

[16] Z. Li, K. Ghia, Y. Li, Z. Fan, and L. Shen, "Unsteady Reynolds-averaged Navier–Stokes investigation of free surface wave impact on tidal turbine wake," *Proceedings of the Royal Society A*, vol. 477, no. 2246, p. 20200703, 2021.

[17] S. Draycott, J. Steynor, A. Nambiar, B. Sellar, and V. Venugopal, "Rotational sampling of waves by tidal turbine blades," *Renewable Energy*, vol. 162, pp. 2197–2209, 2020.

[18] B. Cao, "Hydrodynamic design of multi-rotor tidal array," Ph.D. dissertation, University of Oxford, 2020.

[19] J. Schluntz and R. H. J. Willden, "The effect of blockage on tidal turbine rotor design and performance," *Renewable Energy*, vol. 81, pp. 432–441, 2015.

[20] J. McNaughton, B. Cao, A. Nambiar, T. Davey, C. R. Vogel, and R. H. Willden, "Constructive interference effects for tidal turbine arrays," *Journal of Fluid Mechanics*, vol. 943, p. A38, 2022.

[21] A. Wimshurst, "Tip flow corrections for horizontal axis wind and tidal turbine rotors," Ph.D. dissertation, University of Oxford, 2018.

[22] E. Jost, L. Klein, H. Leipprand, T. Lutz, and E. Krämer, "Extracting the angle of attack on rotor blades from CFD simulations," *Wind Energy*, vol. 21, no. 10, pp. 807–822, 2018.

[23] F. Zilic de Arcos, C. Vogel, and R. Willden, "Extracting angles of attack from blade-resolved rotor CFD simulations," *Wind Energy*, vol. 23, no. 9, pp. 1868–1885, 2020.

[24] M. Zormpa, F. Zilic de Arcos, X. Chen, C. R. Vogel, and R. H. J. Willden, "The effect of flow sampling on the robustness of the actuator line method," *Wind Energy*, 2023, to be submitted.

[25] J. N. Sorensen and W. Z. Shen, "Numerical modeling of wind turbine wakes," *Journal of Fluids Engineering*, vol. 124, no. 2, pp. 393–399, 2002.

[26] A. R. Meyer Forsting, G. R. Pirrung, and N. Ramos-García, "A vortex-based tip/smearing correction for the actuator line," *Wind Energy Science*, vol. 4, no. 2, pp. 369–383, 2019.

[27] B. E. Larsen and D. R. Fuhrman, "On the over-production of turbulence beneath surface waves in Reynolds-averaged Navier–Stokes models," *Journal of Fluid Mechanics*, vol. 853, p. 419–460, 2018.

[28] F. R. Menter, "Two-equation eddy-viscosity turbulence models for engineering applications," *AIAA journal*, vol. 32, no. 8, pp. 1598–1605, 1994.

[29] C. Windt, J. Davidson, P. Schmitt, and J. V. Ringwood, "On the assessment of numerical wave makers in CFD simulations," *Journal of Marine Science and Engineering*, vol. 7, no. 2, p. 47, 2019.

[30] P. Ouro, L. Ramírez, and M. Harrold, "Analysis of array spacing on tidal stream turbine farm performance using large-eddy simulation," *Journal of Fluids and Structures*, vol. 91, p. 102732, 2019.

[31] N. G. Jacobsen, D. R. Fuhrman, and J. Fredsøe, "A Wave Generation Toolbox for the Open-Source CFD Library: OpenFoam®," *International Journal for Numerical Methods in Fluids*, vol. 70, no. 9, pp. 1073–1088, 2012.

[32] M. Borsboom and N. G. Jacobsen, "A generating-absorbing boundary condition for dispersive waves," *International Journal for Numerical Methods in Fluids*, vol. 93, no. 8, pp. 2443–2467, 2021.

[33] J. Fenton, "The numerical solution of steady water wave problems," *Computers & Geosciences*, vol. 14, no. 3, pp. 357–368, 1988.